Mon. Not. R. Astron. Soc. **392,** 1456–1466 (2009) doi:10.1111/j.1365-2966.2008.14158.x

The Monitor project: rotation periods of low-mass stars in M50

Jonathan Irwin,[1,2]★ Suzanne Aigrain,[3] Jerome Bouvier,[4] Leslie Hebb,[5] Simon Hodgkin,[1] Mike Irwin[1] and Estelle Moraux[4]

[1]*Institute of Astronomy, University of Cambridge, Madingley Road, Cambridge CB3 0HA*
[2]*Harvard-Smithsonian Center for Astrophysics, 60 Garden Street, Cambridge, MA 02138, USA*
[3]*Astrophysics Group, School of Physics, University of Exeter, Stocker Road, Exeter EX4 4QL*
[4]*Laboratoire d'Astrophysique, Observatoire de Grenoble, BP 53, F-38041 Grenoble Cédex 9, France*
[5]*School of Physics and Astronomy, University of St Andrews, North Haugh, St Andrews KY16 9SS*

Accepted 2008 October 28. Received 2008 October 21; in original form 2008 September 23

ABSTRACT

We report on the results of a time-series photometric survey of M50 (NGC 2323), a ∼130 Myr open cluster, carried out using the Cerro Tololo Inter-American Observatory (CTIO) 4-m Blanco telescope and Mosaic-II detector as part of the Monitor project. Rotation periods were derived for 812 candidate cluster members over the mass range $0.2 \lesssim M/\mathrm{M}_\odot \lesssim 1.1$. The rotation period distributions show a clear mass-dependent morphology, statistically indistinguishable from those in NGC 2516 and M35 taken from the literature. Due to the availability of data from three observing runs separated by ∼10 and 1 month time-scales, we are able to demonstrate clear evidence for evolution of the photometric amplitudes, and hence spot patterns, over the 10 month gap. We are not able to constrain the time-scales for these effects in detail due to limitations imposed by the large gaps in our sampling, which also prevent the use of the phase information.

Key words: techniques: photometric – surveys – stars: pre-main-sequence – stars: rotation – open clusters and associations: individual: M50.

1 INTRODUCTION

M50 is a populous (∼2100 stars brighter than $V \sim 23$; Kalirai et al. 2003) open cluster of comparable age to the Pleiades, at a moderate distance. We adopt the parameters of Kalirai et al. (2003) for the remainder of this work: a main-sequence turn-off age of 130 Myr, distance 1000^{+81}_{-75} pc and reddening $E(B-V) = 0.22$ mag (an average of the values from Claria, Piatti & Lapasset 1998 and Hoag et al. 1967; see Kalirai et al. 2003). For comparison, the classical main-sequence turn-off age for the Pleiades is 100 Myr (Meynet, Mermilliod & Maeder 1993).

Despite having a very favourable angular size for CCD observations, there are only two previous CCD-based studies of the cluster population in the literature, from Kalirai et al. (2003) and Sharma et al. (2006), obtaining similar values for the cluster parameters. We have undertaken a time-domain photometric survey of M50 with the joint aims of searching for eclipses due to stellar, brown dwarf and planetary companions orbiting low-mass cluster member stars, and to obtain a large sample of rotation periods to study the evolution of stellar angular momentum in conjunction with previous measurements in the literature.

In addition to studying angular momentum evolution, we can also begin to constrain the effects of other cluster parameters such as metallicity and environment on the rotation period distributions, by comparing the M50 distribution with data for clusters of comparable age. Large samples of period measurements are available in NGC 2516 (∼150 Myr; Jeffries, Thurston & Hambly 2001) from Irwin et al. (2007b), covering $0.15 \lesssim M/\mathrm{M}_\odot \lesssim 0.7$, and M35 (also ∼150 Myr; Barrado y Navascués, Deliyannis & Stauffer 2001) from Meibom, Mathieu & Stassun (2008), covering masses down to $\sim 0.6\,\mathrm{M}_\odot$. Although there are relatively few rotation periods measured, especially for M-dwarfs, in the Pleiades, a large sample of $v \sin i$ measurements is available covering masses down to $\sim 0.3\,\mathrm{M}_\odot$ (Stauffer et al. 1984; Stauffer & Hartmann 1987; Soderblom et al. 1993; Jones, Fischer & Stauffer 1996; Queloz et al. 1998; Terndrup et al. 2000), which can be compared to the rotation periods in a statistical sense.

The rotational evolution of low-mass stars on the pre-main-sequence (PMS) is dominated by stellar contraction, with angular momentum thought to be regulated by processes relating to the star–disc interaction (e.g. accretion-driven winds; Matt & Pudritz 2005, or 'disc locking'; Königl 1991; Collier Cameron, Campbell & Quaintrell 1995), giving rise to a spread in rotation rates determined predominantly by the disc lifetime (e.g. Bouvier et al. 1997; Krishnamurthi et al. 1997; Sills, Pinsonneault & Terndrup 2000). As the stars arrive on the zero-age main sequence (ZAMS), the stellar contraction ceases, and angular momentum losses via magnetized stellar winds dominate the subsequent evolution. Observations indicate that the rotation rates of solar-type stars between the age of the

★E-mail: jmi@ast.cam.ac.uk

Hyades (∼625 Myr; Perryman et al. 1998) and the age of the Sun are well described by $\omega \propto t^{-1/2}$, the famous Skumanich (1972) law (e.g. Soderblom 1983). This can be reproduced in a more theoretically motivated framework from parametrized angular momentum loss laws (usually based on Kawaler 1988).

Observations of the Pleiades and other young clusters at ∼50–100 Myr represent a 'snapshot' of the rotational evolution process at the point where solar-type stars have recently reached the ZAMS, and before significant angular momentum losses due to stellar winds have taken place. These indicate that although the evolution of the slowest rotators from this age to the age of the Hyades (and the Sun) can be reproduced by the Skumanich (1972) law, these clusters show a spread in rotation rates at a given mass, and a number of 'ultrafast rotators' (e.g. Soderblom et al. 1993), neither of which are seen in the Hyades and at older ages: here the rotation rate is typically found to follow a fairly well defined function of mass (e.g. Radick et al. 1987). In order to reproduce the ultrafast rotators on the ZAMS, most modellers modify the Kawaler (1988) formalism to incorporate saturation of the angular momentum losses above a critical angular velocity $\omega_{\rm sat}$ (Stauffer & Hartmann 1987; Barnes & Sofia 1996). The saturation is further assumed to be mass dependent, to account for the mass-dependent spin-down time-scales observed on the early main sequence.

There is mounting evidence in the literature that this picture of angular momentum evolution is still not sufficient to reproduce the observations on the ZAMS, in particular over the interval between ∼50 and 500 Myr, if we assume the stars rotate as solid bodies. The observations indicate that such models produce a spin-down over this age range that is too rapid, particularly for the slowest rotators in open clusters (e.g. Irwin et al. 2007b). Several studies (e.g. Krishnamurthi et al. 1997; Allain 1998; Irwin et al. 2007b) have invoked core–envelope decoupling, where the radiative core and convective envelope of the star are allowed to have different rotation rates, as a means to produce a more shallow evolution, by coupling angular momentum from a rapidly spinning core (which experiences little angular momentum loss assuming the disc and wind couple predominantly to the outer convective regions of the star) to the convective envelope on time-scales of a few 100 Myr to provide a 'late time replenishment' of the surface rotation rate.

Open clusters of 50–500 Myr age represent an ideal testing ground for these models. The rotational evolution is strongly mass dependent, so in order to decouple the mass effect from the time-dependence, extremely large sample sizes are required, such that we can obtain good statistics over small bins in mass. M50 represents an ideal target for such a study, having a large population over a relatively small area of sky, which can be observed very efficiently using the multiplex advantage afforded by a standard wide-field CCD mosaic.

The remainder of the paper is structured as follows. The observations and data reduction are described in Section 2, and the colour–magnitude diagram (CMD) of the cluster and candidate membership selection are presented in Section 3. The method we use for obtaining photometric periods is summarized in Section 4 (see Irwin et al. 2006 for a more detailed discussion). Our results are given in Section 5 and Section 6 summarizes our conclusions.

2 OBSERVATIONS AND DATA REDUCTION

Photometric monitoring observations were obtained as part of the Monitor project (Aigrain et al. 2007), using the 4-m Blanco telescope at Cerro Tololo Inter-American Observatory (CTIO), with the Mosaic-II imager. This instrument provides a field of view (FoV) of ∼36 × 36 arcmin^2 (0.37 deg^2), using a mosaic of eight 2048 × 4096 pixel CCDs, at a scale of ∼ 0.27 arcsec pixel^{-1}. A total of ∼95 h of photometric monitoring was conducted, spread over three distinct observing runs: 6× full-nights in two three-night segments spanning 2005 February 04–06 and 2005 February 14–16, 8 × 1/2 nights between 2005 December 24 and 2006 January 06 and 4× full-nights between 2006 January 28 and 2006 February 01. M50 was observed in a single telescope pointing centred on the cluster, for ∼8 h per night (∼4 h per 1/2 night), in parallel with another field in the cluster NGC 2362, the results from which were published in Irwin et al. (2008b). Exposure times were 75 s in *i* band, giving a cadence of ∼6 min (composed of 2 × 75 s exposures plus 2 × 100 s readout time, slewing between M50 and NGC 2362 during readout). We also obtained deep *V*-band exposures (2 × 600, 450 and 150 s), which were stacked and used to produce a CMD of the cluster.

For a full description of our data reduction steps, the reader is referred to Irwin et al. (2007a). Briefly, we used the pipeline for the Isaac Newton Telescope (INT) wide-field survey (Irwin & Lewis 2001) for 2D instrumental signature removal (bias correction, flat-fielding, defringing) and astrometric and photometric calibration. We then generated a master catalogue for each filter by stacking 20 of the frames taken in the best conditions (seeing, sky brightness and transparency) and running the source detection software on the stacked image. The resulting source positions were used to perform aperture photometry on all of the time-series images. We achieved a per data point photometric precision of ∼2–4 mmag for the brightest objects, with rms scatter <1 per cent for $i \lesssim 19$ (see Fig. 1). A signal-to-noise ratio of 5 (corresponding approximately to the detection limit for point sources on a single frame of the differential photometry) is reached at $i \sim 22.7$.

Our source detection software flags any objects detected as having overlapping isophotes. This information is used, in conjunction with a morphological image classification flag also generated by the pipeline software (Irwin & Lewis 2001), to allow us to identify non-stellar or blended objects in the time-series photometry.

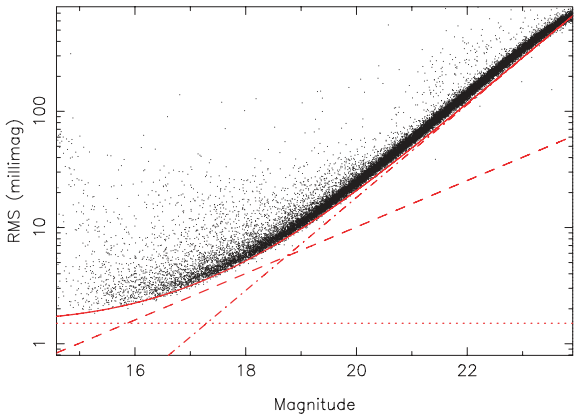

Figure 1. Plot of rms scatter per data point (measured over the entire data set) as a function of magnitude for the *i*-band observations of a single field in M50, for all unblended objects with stellar morphological classifications. The diagonal dashed line shows the expected rms from Poisson noise in the object, the diagonal dot–dashed line shows the rms from sky noise in the photometric aperture and the dotted line shows an additional 1.5 mmag contribution added in quadrature to account for systematic effects. The solid line shows the overall predicted rms, combining these contributions.

Photometric calibration of our data was carried out using regular observations of Landolt (1992) equatorial standard star fields in the usual way.

Light curves were extracted from the data for ∼63 000 objects, 42 000 of which had stellar morphological classifications (∼23 per cent of these are flagged as having overlapping isophotes by the source detection software, and thus may be blended), using our standard aperture photometry techniques, described in Irwin et al. (2007a). We fit a 2D quadratic polynomial to the residuals in each frame (measured for each object as the difference between its magnitude on the frame in question and the median calculated across all frames) as a function of position, for each of the eight CCDs separately. Subsequent removal of this function accounts for effects such as varying differential atmospheric extinction across each frame. Over a single CCD, the spatially varying part of the correction remains small, typically ∼0.02 mag peak-to-peak. The reasons for using this technique are discussed in more detail in Irwin et al. (2007a).

For the production of deep CMDs, we stacked 20 i-band observations, taken in good seeing and photometric conditions, and all of the V-band observations. The limiting magnitudes on these stacked images, measured as the approximate magnitude at which our catalogues are 50 per cent complete, were $V \simeq 24.4$ and $i \simeq 23.6$.

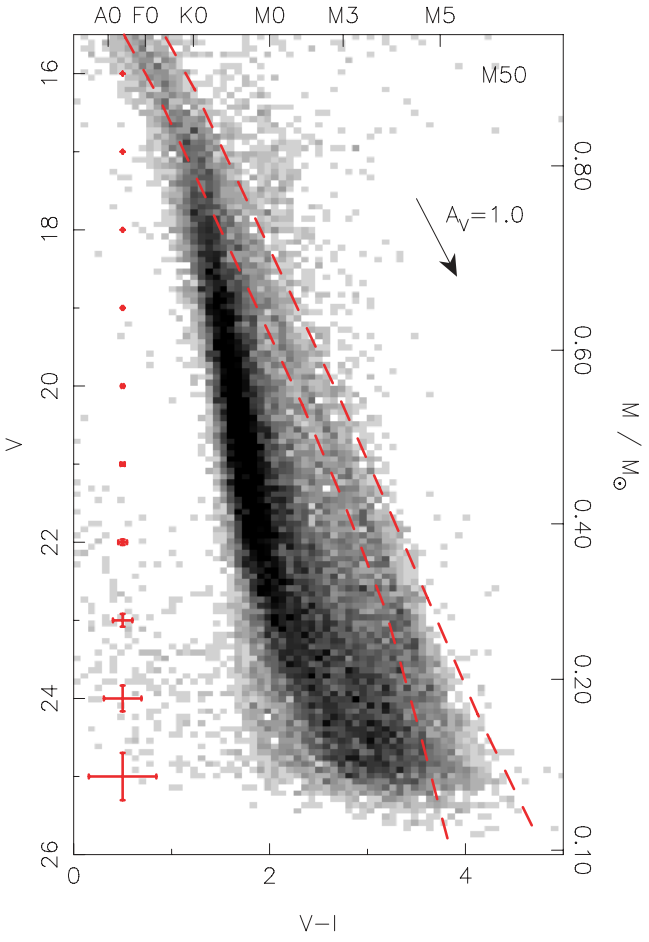

Figure 2. V versus $V - I$ CMD of M50 from stacked images plotted as a 'Hess diagram' (grey-scale map of the number density of sources in 0.1 mag bins), for all objects with stellar morphological classification. The cluster sequence is clearly visible on the right-hand side of the diagram. The boundaries of the region used to select photometric candidate members are shown by the dashed lines (all objects between the dashed lines were selected). The reddening vector for $A_V = 1.0$ is shown at the right-hand side of the diagram. The mass scale is from the NextGen models of Baraffe et al. (1998), interpolated to 130 Myr, using our empirical isochrone to convert the V magnitudes to I magnitudes, and subsequently obtaining the masses from these, due to known problems with the V magnitudes from the models (see e.g. Baraffe et al. 1998). The error bars at the left-hand side of the plot indicate the typical photometric error for an object on the cluster sequence.

3 SELECTION OF CANDIDATE LOW-MASS MEMBERS

3.1 The V versus $V - I$ CMD

Our CMD of M50 is shown in Fig. 2. The V and i measurements were converted to the standard Johnson–Cousins photometric system using colour equations derived from our standard star observations:

$$(V - I) = (V_{\rm ccd} - i_{\rm ccd})/0.899 \quad (1)$$

$$V = V_{\rm ccd} + 0.005\,(V - I) \quad (2)$$

$$I = i_{\rm ccd} - 0.096\,(V - I). \quad (3)$$

Candidate cluster members were selected by defining an empirical cluster sequence 'by eye' to follow the clearly visible cluster single-star sequence. The cuts were defined by moving this line along a vector perpendicular to the cluster sequence, by amounts $k - \sigma(V - I)$ and $k + \sigma(V - I)$ as measured along this vector, where $\sigma(V - I)$ is the photometric error in the $V - I$ colour. The values of k used were -0.125 mag for the lower line and 0.25 mag for the upper line on the diagram, making the brighter region wider to avoid rejecting binary and multiple systems, which are overluminous for their colour compared to single stars. 4249 candidate photometric members were selected, over the full V magnitude range from $V =$ 15.5 to 26, but the cluster sequence becomes difficult to distinguish from the field population for $V \gtrsim 24$ ($M \lesssim 0.2\,{\rm M}_\odot$).

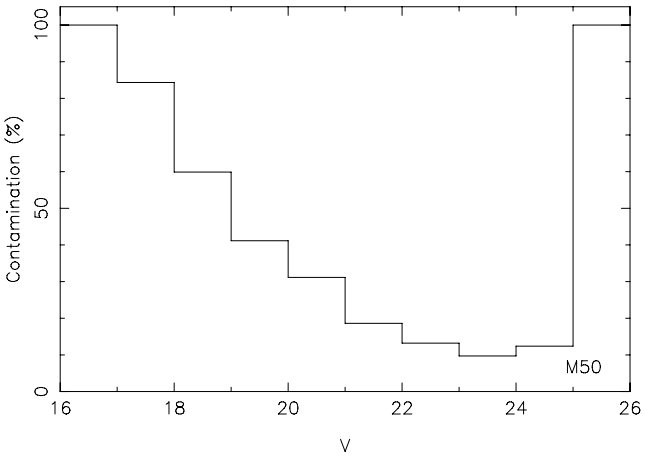

Figure 3. Contamination estimated from Galactic models, measured as the ratio of the calculated number of objects in each magnitude bin from the models, to the number of objects detected and classified as candidate cluster members in that magnitude bin. Note that bins with contamination estimates > 100 per cent (where there were more objects in that bin from the Galactic model than were actually observed) have been truncated to 100 per cent.

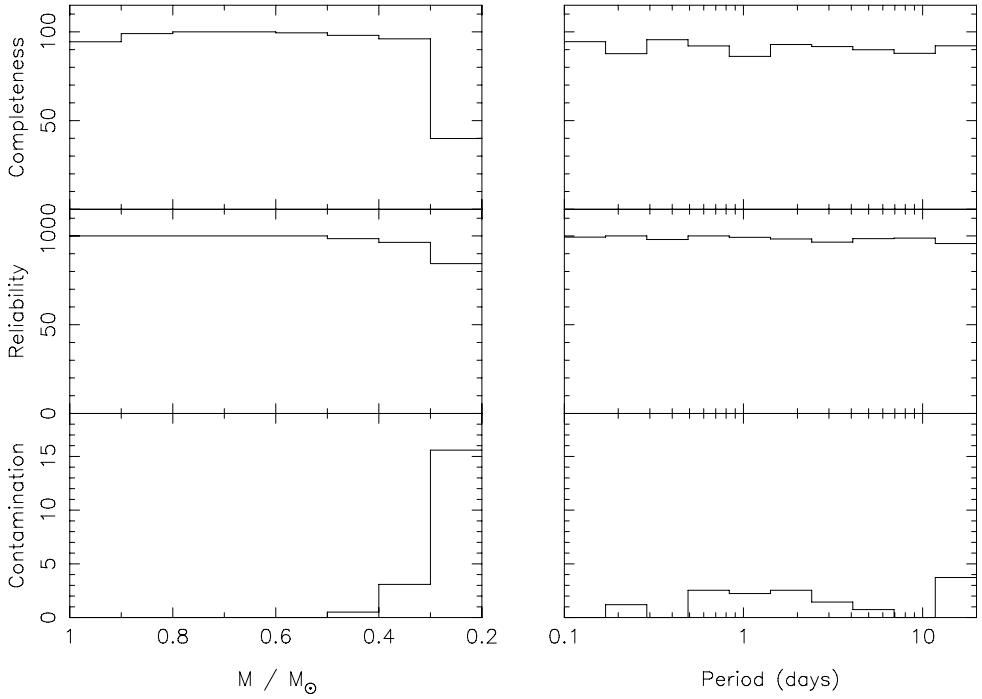

Figure 4. Results of the simulations for 0.02 mag amplitude expressed as percentages, plotted as a function of mass (left-hand panel) and period (right-hand panel). The simulated region covered $0.1 < M/\mathrm{M}_\odot < 1.0$ in order to be consistent with the M50 sample. Top panels: completeness as a function of real (input) period. Centre panels: reliability of period determination, plotted as the fraction of objects with a given true period, detected with the correct period (defined as differing by <20 per cent from the true period). Bottom panels: contamination, plotted as the fraction of objects with a given detected period, having a true period differing by > 20 per cent from the detected value.

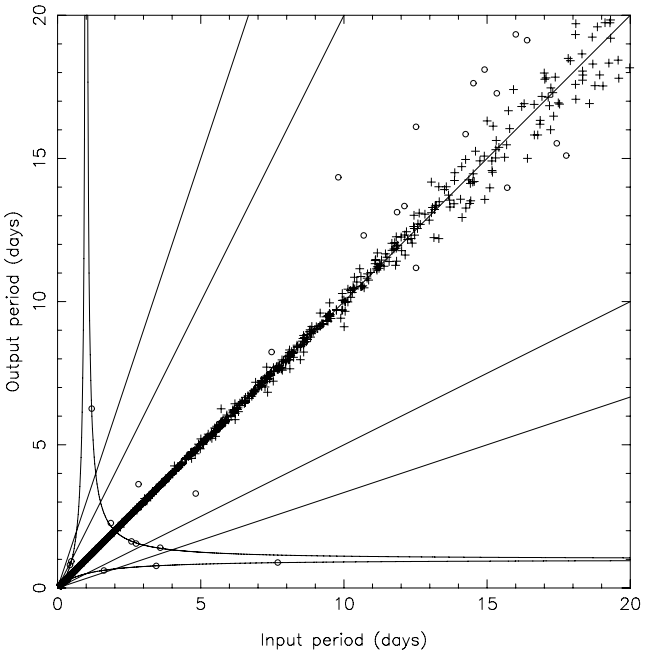

Figure 5. Detected period as a function of actual (input) period for our simulations. Objects plotted with crosses had fractional period error <10 per cent, open circles > 10 per cent. The straight lines represent equal input and output periods, and factors of 2, 3, 1/2 and 1/3. The curved lines are the loci of the $\pm 1\,\mathrm{d}^{-1}$ aliases resulting from gaps during the day. The majority of the points fall on (or close to) the line of equal periods.

In this and subsequent sections, we make use of mass estimates for the cluster members. These were derived from the *I*-band absolute magnitudes and the models of Baraffe et al. (1998), interpolated to 130 Myr age. We did not use the $V - I$ colour due to known problems with the *V*-band magnitudes from the models (see Baraffe et al. 1998).

3.2 Contamination

Since the cluster sequence is not well separated from the field in the CMD, it is important to estimate the level of field star contamination in the sample of candidate cluster members. In this work, we have used Galactic models to obtain a simple first estimate of the contamination level. This will be refined using spectroscopic follow-up observations in a later publication.

The Besançon Galactic models (Robin et al. 2003) were used to generate a simulated catalogue of objects passing our selection criteria at the Galactic coordinates of M50 ($l = 221\overset{\circ}{.}7$, $b = -1\overset{\circ}{.}3$), covering the total FoV of $\sim$0.35 deg^2 (including gaps between detectors). The same selection process as above for the cluster members was applied to this catalogue to find the contaminant objects. A total of 1970 simulated objects passed these membership selection criteria, giving an overall contamination level of $\sim$47 per cent after correcting for bins where the number of objects predicted by the models exceeded the number actually observed (we simply assumed 100 per cent field contamination in these bins.). Fig. 3 shows the contamination as a function of *V* magnitude. Note that this figure should be treated with extreme caution due to the need to use Galactic models, and especially given the overestimation of the numbers of observed objects by the models.

4 PERIOD DETECTION

4.1 Method

The method we use for the detection of periodic variables was described in detail in Irwin et al. (2006). It uses least-squares fitting of sine curves to the time series $m(t)$ (in mag) for all candidate cluster members, using the form

$$m(t) = m_{\rm dc} + \alpha \sin(\omega t + \phi), \quad (4)$$

where $m_{\rm dc}$ (the DC light curve level), α (the amplitude) and ϕ (the phase) are free parameters at each value of ω over an equally spaced grid of frequencies, corresponding to periods from 0.05 to 50 d for the present data set.

For M50, we modified this to fit separate coefficients $m_{\rm dc}$, α and ϕ for each of the three observing runs (a total of nine coefficients at each value of ω) to allow for changes in the spot patterns that give rise to the observed photometric modulations. The period was required to remain the same over all the observing runs, which is expected since it should represent the underlying rotation period of the star, and this will change by a negligible amount due to rotational evolution over only 1 yr. This procedure is necessary for such a long data set since significant evolution of the spot coverage of our targets is expected over time-scales shorter than 1 yr.

Periodic variable light curves were selected as before by evaluating the change in reduced χ^2:

$$\Delta\chi^2_\nu = \chi^2_\nu - \chi^2_{\nu,\rm smooth} > 0.4, \quad (5)$$

where χ^2_ν is the reduced χ^2 of the original light curve with respect to a constant model, and $\chi^2_{\nu,\rm smooth}$ is the reduced χ^2 of the light curve with a smoothed, phase-folded version subtracted. Again, $\chi^2_{\nu,\rm smooth}$ was calculated for the three observing runs separately, and then summed, to account for any evolution in amplitude and/or phase. Since fitting for separate $m_{\rm dc}$ coefficients in each observing run renders the period search insensitive to very long period modulations appearing as simple 'DC offsets' between the runs, we evaluated χ^2_ν for a three constant model, where we allowed for a different constant light curve level in each observing run.

The threshold of $\Delta\chi^2_\nu > 0.4$ was used for the M34 data and appears to work well here too, checked by examining all of the light curves for two of the detectors, chosen randomly. A total of 1700 objects were selected by this automated part of the procedure. These light curves were then examined by eye, to define the final sample of periodic variables. A total of 812 light curves passed this final stage, where the remainder had spurious variability (caused by systematic effects) or were too ambiguous to be included.

4.2 Simulations

Simulations were performed following the method detailed in Irwin et al. (2006), injecting simulated signals of 2 per cent amplitude and periods chosen following a uniform distribution on $\log_{10}$ period from 0.1 to 20 d, into light curves covering a uniform distribution in mass, from 1.0 to 0.1 $M_\odot$. A total of 2111 objects were simulated. The phase of the modulations was randomized for each observing run in order to provide a more realistic evaluation of the sensitivity of our method across changes in spot patterns.

The results of the simulations are shown in Fig. 4 as diagrams of completeness, reliability and contamination as a function of period and stellar mass. Broadly, our period detections are close to 100 per cent complete for these amplitudes from 1.0 $M_\odot$ down to 0.3 $M_\odot$, with remarkably little period dependence. At the very lowest masses (particularly in the $0.2 < M/M_\odot < 0.3$ bin of the diagram), the completeness drops substantially, and the reliability of the detected periods deteriorates slightly, due to the increased noise level in the light curves. For $M < 0.2\,M_\odot$, the completeness drops essentially to zero for 2 per cent modulations.

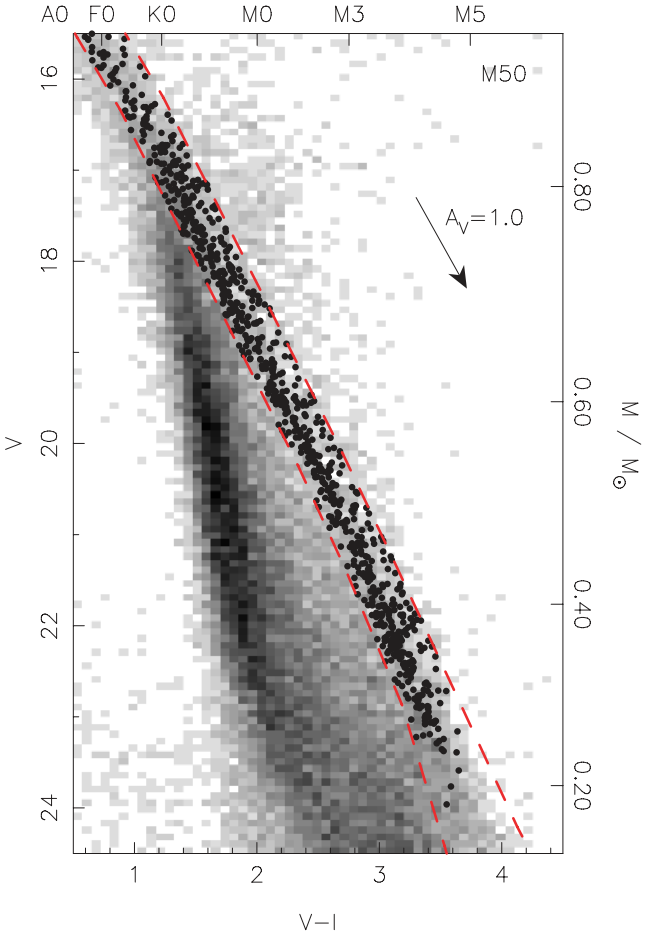

Figure 6. Magnified V versus $V - I$ CMD of M50, for objects with stellar morphological classification, as Fig. 2, showing all 812 candidate cluster members with detected periods (black points). The dashed lines show the cuts used to select candidate cluster members (see Section 3.1).

Fig. 5 shows a comparison of the detected periods with real periods for our simulated objects, indicating good reliability of period recovery, with only a small amount of aliasing, especially when compared to some of our previous data sets (e.g. M34; Irwin et al. 2006), presumably due to the extended time-coverage of the M50 observations.

5 RESULTS

The locations of our detected periodic variable candidate cluster members on a V versus $V - I$ CMD of M50 are shown in Fig. 6. The diagram indicates that the majority of the detections lie on the single-star cluster sequence, as would be expected for rotation in cluster stars as opposed to, say, eclipsing binaries.

The properties of all our rotation candidates are listed in Table 1.

5.1 M50 rotation periods

Plots of period as a function of $V - I$ colour and mass for the photometrically selected candidate cluster members are shown in

Table 1. Properties of our 812 rotation candidates, including V- and I-band magnitudes and uncertainties from our CCD photometry, the period P, i-band amplitudes $\alpha_1, \alpha_2, \alpha_3$ and uncertainties (magnitudes, in the instrumental bandpass), interpolated mass and radius (from the models of Baraffe et al. 1998, derived using the I magnitudes). In the table, $\sigma(x)$ denotes the uncertainty in quantity x. Note that these uncertainties do not incorporate systematic errors (e.g. in the zero-point calibration) that dominate at the bright end. Our identifiers are formed using a simple scheme of the cluster name, CCD number and a running count of stars in each CCD, concatenated with dashes. The full table is available as Supporting Information in the online version of the journal. Machine-readable copies of the data tables from all the Monitor rotation period publications are also available at http://www.ast.cam.ac.uk/research/monitor/rotation/.

Identifier	RA J2000	Dec. J2000	V (mag)	$\sigma(V)$ (mag)	I (mag)	$\sigma(I)$ (mag)	P (days)	α_1 (mag)	$\sigma(\alpha_1)$ (mag)	α_2 (mag)	$\sigma(\alpha_2)$ (mag)	α_3 (mag)	$\sigma(\alpha_3)$ (mag)	M ($M_\odot$)	R ($R_\odot$)
M50-1-98	07 01 35.53	−08 33 10.6	17.082	0.001	15.911	0.001	12.807	0.0091	0.0003	0.0035	0.0002	0.0115	0.0011	0.81	0.76
M50-1-413	07 01 38.56	−08 34 35.7	21.993	0.015	18.950	0.007	0.741	0.0078	0.0010	0.0209	0.0011	0.0229	0.0012	0.37	0.36
M50-1-651	07 01 40.52	−08 33 28.3	16.521	0.001	15.423	0.001	6.811	0.0055	0.0002	0.0063	0.0002	0.0024	0.0004	0.88	0.84
M50-1-979	07 01 43.77	−08 32 58.5	21.901	0.014	18.710	0.006	0.865	0.0189	0.0009	0.0108	0.0009	0.0104	0.0014	0.41	0.39
M50-1-1130	07 01 45.15	−08 34 11.0	21.330	0.009	18.538	0.006	0.924	0.0138	0.0014	0.0173	0.0008	0.0292	0.0013	0.44	0.41

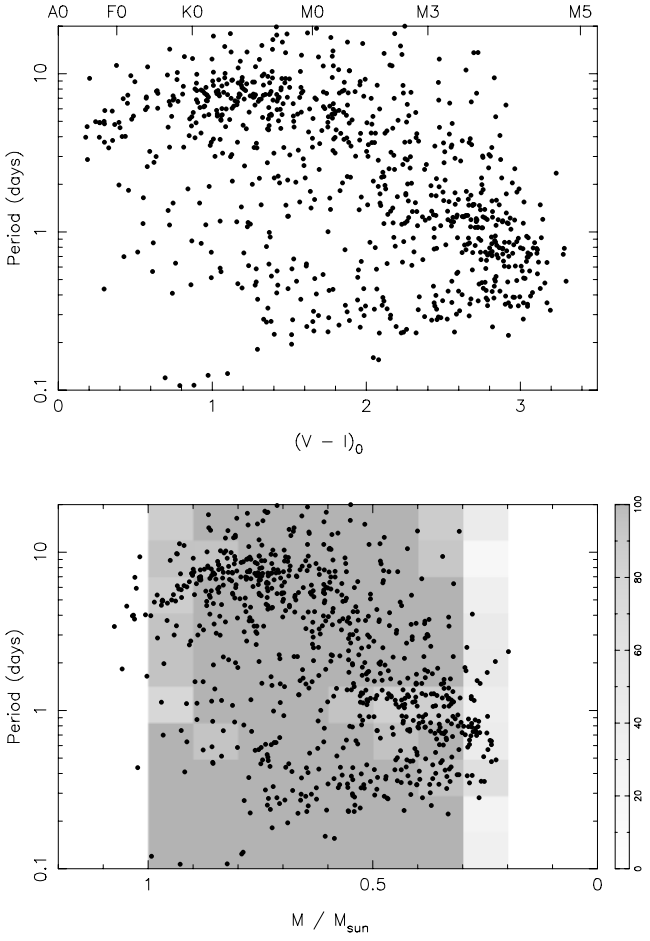

Figure 7. Plots of rotation period as a function of dereddened $V - I$ colour (top), and mass (bottom) for M50, deriving the masses using the 130 Myr NextGen mass–magnitude relations of Baraffe et al. (1998) and our measured I-band magnitudes. In the lower diagram, the grey-scales show the completeness for 0.02 mag periodic variations from the simulations.

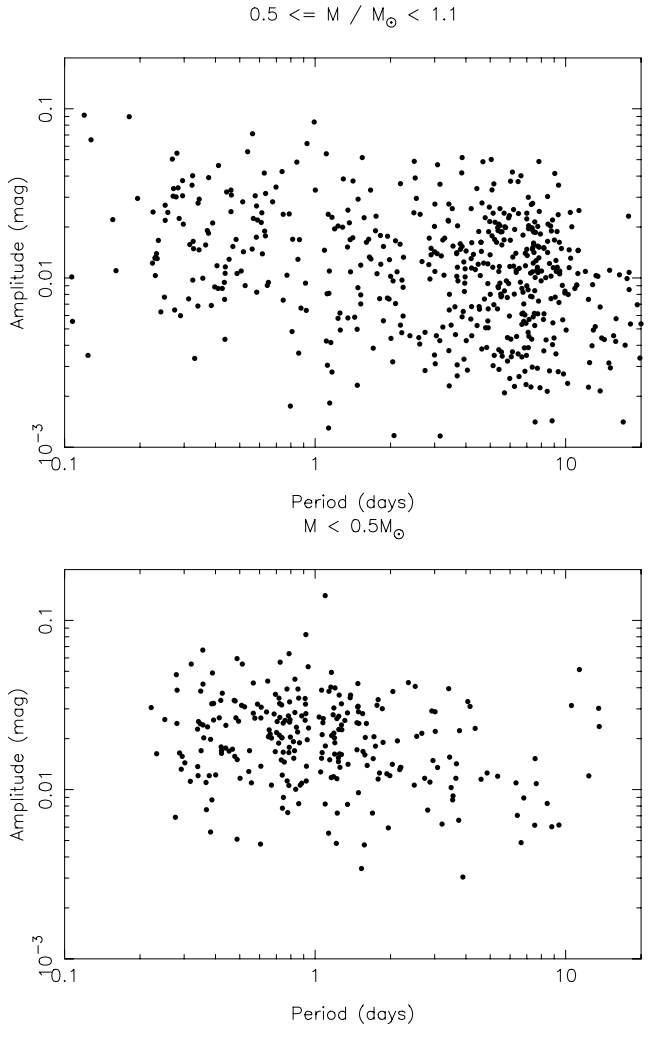

Figure 8. Plot of amplitude as a function of period for M50 in two mass bins: $0.5 \leq M/M_\odot < 1.1$ (top) and $M < 0.5\,M_\odot$ (bottom).

Fig. 7. Below $\sim$0.7 $M_\odot$ (or M0), these diagrams reveal a correlation between stellar mass (or spectral type) and the longest rotation period seen at that mass, with a clear lack of slow rotators at very low masses. This trend is also followed by the majority of the rotators in this mass range, with only a tail of faster rotators to $\sim$0.2 day periods, and very few objects rotating faster than this. This is very similar to what we found in the earlier NGC 2516 and NGC 2547 studies (Irwin et al. 2007b, 2008a).

Above $\sim$0.7 $M_\odot$, the M50 data indicate an inverse trend, of decreasing rotation period (faster rotation) as a function of increasing mass. The slope of this relation is much shallower than the one below 0.7 $M_\odot$. The existence of such a relation was noted by Hartman et al. (2008) in M37 ($\sim$550 Myr), and is also clearly

evident in the $v \sin i$ data for NGC 2516 and the Pleiades, and recently published rotation period data in M35 (Meibom et al. 2008), as shown in Fig. 11 (left-hand panel), which will be discussed in Section 5.3.

These morphological features do not appear to be a result of sample biases. In particular, the simulations show that the survey is sensitive to much shorter periods than 0.2 d, and the upper limit in detectable periods is not mass dependent, so this cannot explain the morphology of the upper envelope of rotation periods in Fig. 7. Moreover, the presence of these features in multiple rotation period data sets with differing selection biases, and in $v \sin i$ data, strongly indicates that they are real features of the underlying rotation rate distribution of low-mass stars.

As a further check, we can examine the distribution of rotation periods as a function of amplitude. This is shown in Fig. 8, split into two mass bins. There does not appear to be any clear sensitivity bias, with very low amplitudes being detected over the full range of period, for the $M < 0.5\,\mathrm{M}_{\odot}$ bin.

The higher-mass bin ($0.5 \leq M/\mathrm{M}_{\odot} < 1.1$) appears to show a correlation between amplitude and rotation period, in the sense that longer-period objects show smaller amplitudes. This is confirmed by applying a non-parametric Spearman rank correlation analysis, which gave $r_{\mathrm{s}} = -0.25$, corresponding to a probability of 3×10^{-9} that the quantities are uncorrelated given the sample size. This trend is also present in the lower-mass bin, but at a lower significance level (mostly due to the smaller sample size), with $r_{\mathrm{s}} = -0.22$, and a probability of 4×10^{-4}.

This correlation could be the result of a bias against detection of very small amplitude modulations at short periods, but this is in the opposite sense to the expected trend: it is easier to detect small modulations at short periods since the slope of the light curve within each night is larger, which contributes significantly to our confidence that the variation is real. We speculate that there are two likely causes of the trend we have observed: either this is a result of the well-known relation between rotation rates and stellar activity (e.g. see Güdel 2004, for a review), in the sense that fast rotators are more active, and therefore are more spotted, giving rise to a larger photometric amplitude, or the contamination of our sample by field stars, which are in general less active and more slowly rotating than cluster stars, leads to a population of contaminant objects at the long-period end giving rise to the apparent correlation. The upper panel of Fig. 8 already contains a hint that the latter may be the case: the distribution of amplitudes for periods >10 d appears to be systematically skewed towards smaller amplitudes than that for periods <10 d. Moreover, we expect there to be very few cluster stars rotating more slowly than 10 d at this age from rotational evolution models (e.g. see Irwin et al. 2007b, 2008a,b).

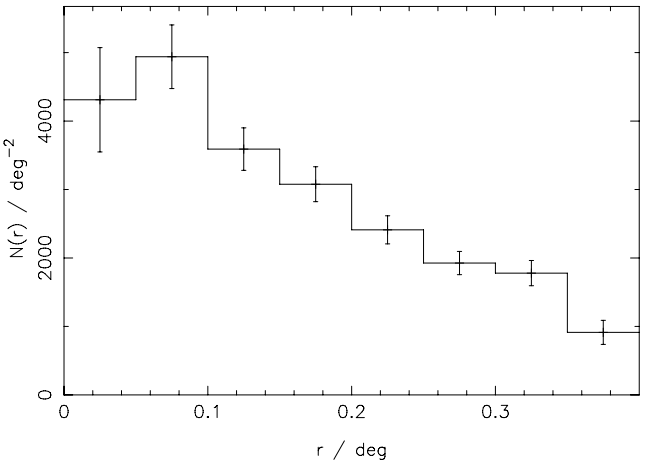

Figure 9. Radial distribution for objects with detected periods. The counts in each annulus have been corrected for the area of sky covered by the CCD mosaic by summing the area of all the pixels falling within that annulus. This correction is only approximate for the outermost regions (e.g. $r \gtrsim 0.^{\circ}35$) since it does not take into account incompleteness in the detections close to the edges of the detector, so the counts in the $0.^{\circ}35 < r < 0.^{\circ}4$ bin in particular may be unreliable. The apparent deficit of objects in the innermost ($r < 0.^{\circ}05$) bin is most likely due to a small error in the position of the cluster centre.

5.2 Radial distribution of periodic variables

In order to further examine the effect of field contamination, we show in Fig. 9 the radial distribution of the detected periodic variable objects, and in Fig. 10 the rotation period distribution as a function of mass in three radial bins, measuring the radius r with respect to the approximate position of the cluster centre. We adopt a position of RA $7^{\mathrm{h}}02^{\mathrm{m}}47^{\mathrm{s}}.4$, Dec. $-8^{\circ}20'43''$ (Sharma et al. 2006; see their table 5). These authors derive a cluster core radius of 6.5 arcmin and a total extent of 17 arcmin, which are broadly consistent with Fig. 9, so we expect field stars to dominate our largest-radius bin in Fig. 10. While this is clearly not the case, given the presence of the same well-defined morphology in rotation period as a function of

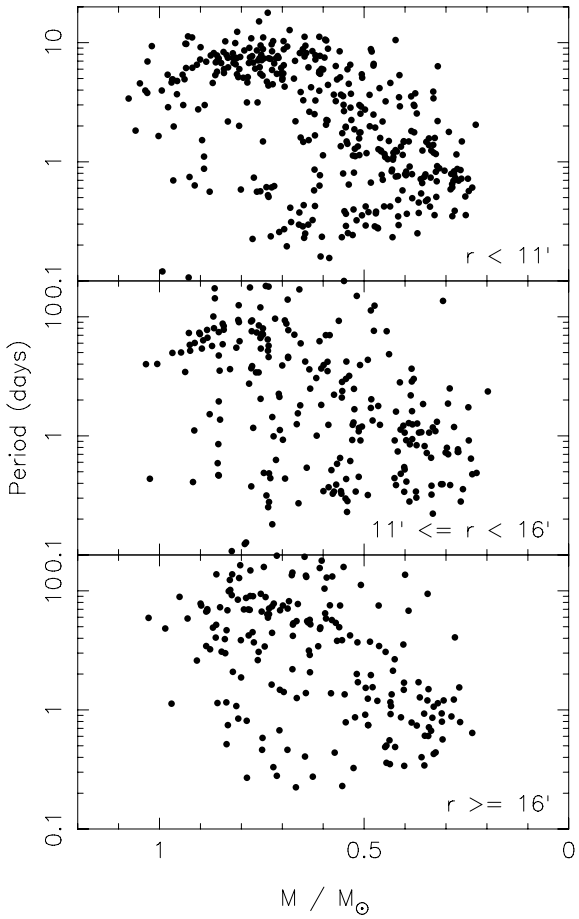

Figure 10. Rotation period as a function of mass, as Fig. 8, plotted in three radial bins of approximately equal area on the sky: $r < 11$ arcmin (top), $11 \leq r < 16$ arcmin (centre) and $r \geq 16$ arcmin (bottom). The latter bin extends to the edge of the $\sim 36 \times 36$ arcmin^2 FoV of our observations.

mass in all the three bins (presumably due to the cluster population), the fraction of objects with periods >10 d does appear to increase with r, becoming especially clear in the bottom panel of the figure. This suggests that these objects may indeed be slowly rotating field stars contaminating the sample.

The existence of a significant population of cluster stars in the lower panel of Fig. 10 is not necessarily inconsistent with the conclusions of Sharma et al. (2006). First, by requiring the objects to have measured rotation periods, we strongly bias the sample in favour of cluster stars, since these are more active. Secondly, many clusters are found to have a larger apparent extent at low masses (e.g. Larson 1982; McNamara & Sekiguchi 1986; Sagar et al. 1988), in some cases even having a 'halo' population of low-mass stars (e.g. h and χ Persei: Schild 1967; Currie et al. 2007). Our rotation period sample probes ∼3 mag deeper in V band than the survey by Sharma et al. (2006), and is therefore dominated by lower-mass stars. The radial distribution shown in the lowest-mass bin of their fig. 4 supports this hypothesis, showing a larger cluster population at large radii than their higher-mass bins. Due to the limited angular coverage of the present survey, it is difficult to confirm this from Fig. 9.

5.3 Comparison with NGC 2516 and M35

By comparing the rotation period distributions in different clusters of the same age, we can begin to constrain the effect of cluster environment, and other parameters such as metallicity, on the distribution of rotation periods. In the case of M50, suitable rotation period samples are available in the literature for NGC 2516 (Irwin et al. 2007b) and M35 (Meibom et al. 2008), with a reasonable overlap in the mass range covered. The metallicity of M50 does not yet appear to have been reported in the literature, but estimates are available for NGC 2516 indicating that it is near-solar ([Fe/H] = -0.05 ± 0.14; Terndrup et al. 2002), and for M35 indicating a sub-solar metallicity ([Fe/H] = -0.21 ± 0.10; Barrado y Navascués et al. 2001). Fig. 11 shows a comparison of the rotation periods measured in these two clusters with the M50 distribution from the present study.

Examining the left-hand panels of Fig. 11 first, the morphology displayed in all the clusters is clearly very similar over the mass ranges in common. The Pleiades $v \sin i$ data appear to show a slightly different 'turn-over' point for the slowest rotators, at ∼0.9 $M_\odot$

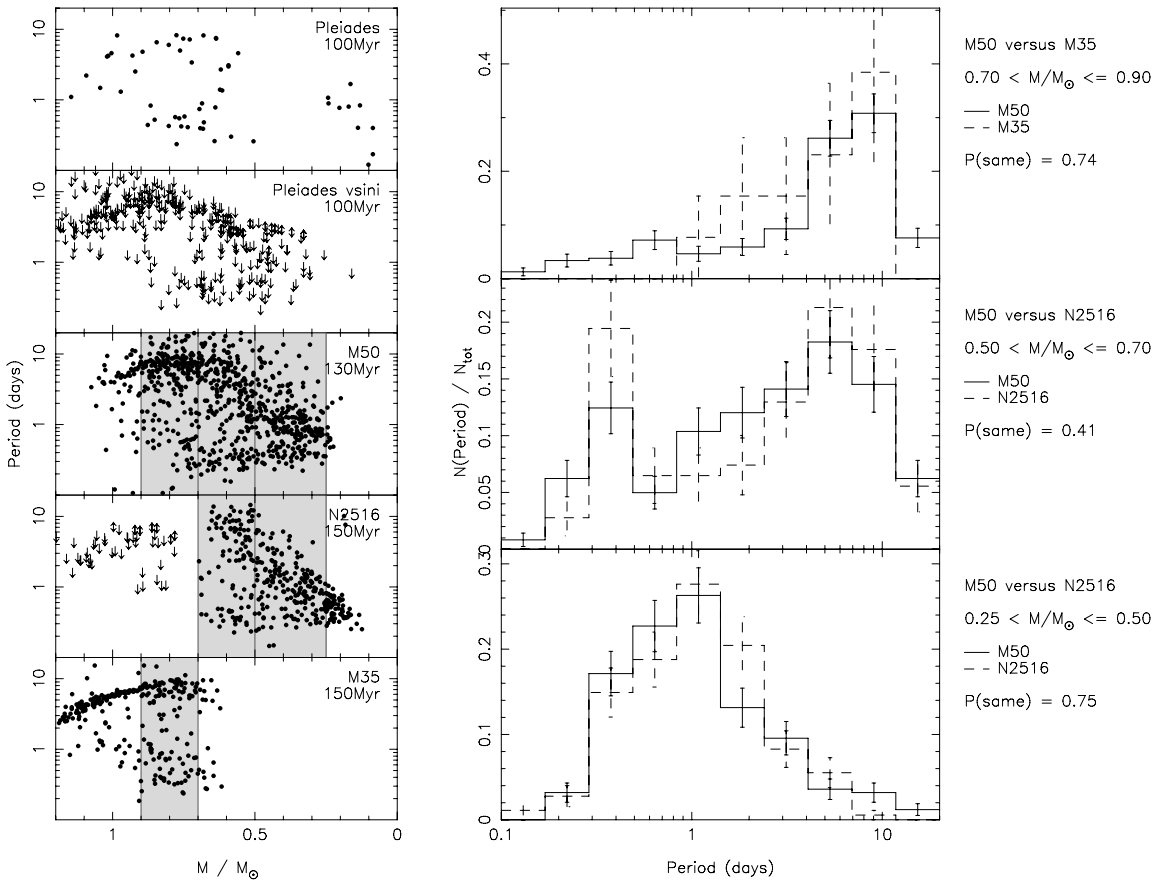

Figure 11. Comparison of the M50 rotation period distribution with rotation period measurements in the Pleiades (Magnitskii 1987; Stauffer 1987 & Van Leeuwen 1987; Prosser et al. 1993a,b, 1995; Krishnamurthi et al. 1998; Terndrup et al. 1999; Scholz & Eislöffel 2004), $v \sin i$ measurements in the Pleiades (Stauffer et al. 1984; Stauffer & Hartmann 1987; Soderblom et al. 1993; Jones et al. 1996; Queloz et al. 1998; Terndrup et al. 2000) and rotation periods in NGC 2516 and M35. Left-hand panel: rotation period as a function of mass for all five samples. Masses were computed using the measured I-band magnitudes, interpolating the models of Baraffe et al. (1998) to the appropriate metallicity and age for each cluster, using the estimates of these parameters from the literature quoted in Sections 1 and 5.3 (for M50, we simply assumed solar metallicity given the lack of an estimate). Right-hand panel: comparison of histograms of rotation period binned in mass to those regions where the cluster samples have sufficient overlap for a meaningful comparison. The grey shaded regions in the left-hand panels indicate the mass ranges used for the histograms on the right-hand panel. Note that these distributions have not been corrected for contamination by field stars due to the lack of follow-up data. Nevertheless, the rotation period distributions in all these clusters are qualitatively very similar, and appear to be statistically indistinguishable given the present sample sizes.

rather than 0.7 $M_{\odot}$ for the other clusters, but this may be the result of the sin *i* ambiguity and the difficulty of detecting the slowest rotating objects via this method. Therefore, qualitatively, the distributions of rotation period versus mass for all the clusters appear to be very similar.

In order to allow a quantitative comparison to be made, we have compared the distributions of rotation periods in three mass bins, chosen to resolve morphological changes in the diagram while concentrating on the regions where the various samples overlap sufficiently to allow a meaningful comparison. These are shown in the right-hand panels of Fig. 11. In all three cases, the distributions are extremely similar, generally differing by less than their combined respective Poisson counting uncertainties. This was confirmed by applying non-parametric two-sided Kolmogorov–Smirnov tests to the distributions, the results of which are given in the figure. In all cases, the distributions are statistically indistinguishable.

The present samples in these three clusters therefore do not show evidence for dependence of rotation on cluster environment, or a 'third parameter' such as metallicity. This is, of course, not conclusive evidence that such a dependence does not exist, especially since the environment and other parameters are relatively similar for the three clusters considered in this work. In order to conduct a more stringent test, additional rotation period observations in a substantially different environment at similar age will be needed.

5.4 Changes in amplitude: evolution of the spot patterns

The availability of three epochs of data corresponding to the three different observing runs allows us to constrain the evolution of the spot patterns giving rise to the photometric modulations, by examining the evolution of the amplitude between the runs. Moreover, by comparing results in multiple clusters (e.g. our NGC 2362 data set, which has the same sampling), we can examine the dependence of the spot evolution rate on cluster age.

Fig. 12 shows histograms of the ratio of the amplitudes between pairs of observing runs. As expected, over the interval between the first two runs (∼10 months), compared to that between the second two runs (∼1 month), the standard deviation of the amplitude ratio is larger, by a factor of ∼1.8, indicating that a larger fraction of the amplitudes evolved over the longer time-span between the first two observing runs. This clearly demonstrates that the spot patterns on our target stars must have evolved over the 10 month gap. The evolution in amplitude is, none the less, relatively modest, which is not surprising since it is reasonable to expect stars of a given activity level to maintain comparable levels of spot coverage over long timescales, with the phase of the modulations evolving according to the short time-scale evolution of individual spots or spot groups.

Unfortunately, for the sampling strategy we have used, we cannot use the phase information to examine this evolution. This arises because the number of cycles of modulation over the ∼10 month gap between the first and second observing runs is large, and unknown. Therefore, small errors in the rotation period, accumulated over the many cycles occurring in the 10 month gap, can lead to large phase shifts between the two observing runs. For example, even a 1 per cent error in a rotation period of 10 days gives rise to a cumulative uncertainty of ∼0.3 cycle after 10 months, and this effect is worse for shorter periods. Fig. 13 illustrates this effect, showing that over the gap between the first and second observing runs, the phase is essentially randomized for 100 per cent of the sample.

Therefore, with the present data set, it is difficult to further constrain the spot lifetimes giving rise to the observed evolution.

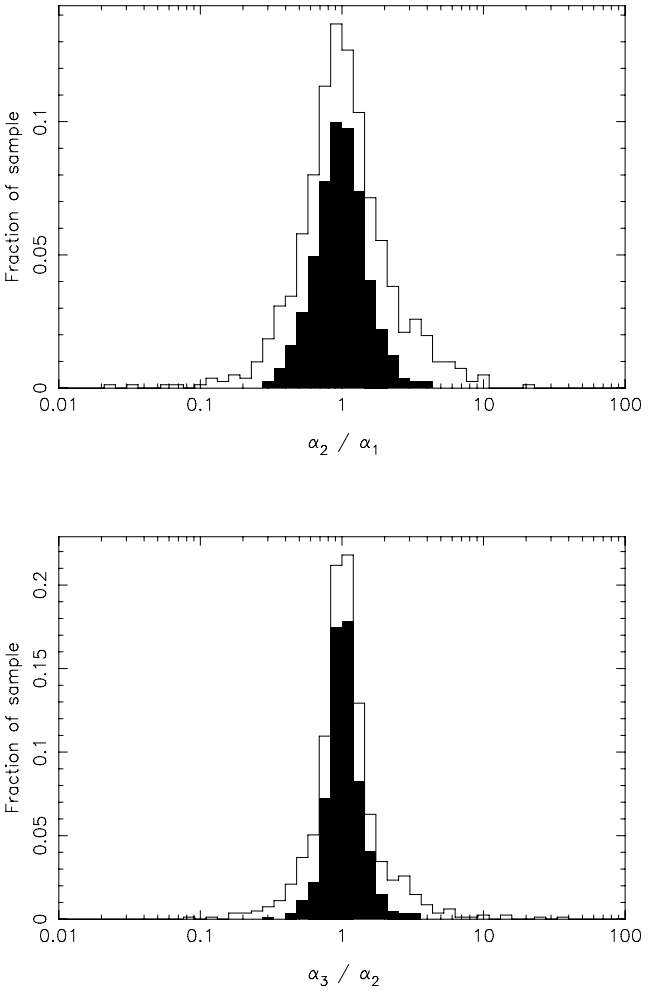

Figure 12. Histograms of the relative amplitudes from the sine curve fitting procedure described in Section 4.1 for the second and first observing runs (upper panel), and the third and second observing runs (lower panel). The mid-points of these were separated by ∼10 months and 1 month, respectively. The open histogram shows the entire sample, and the solid histogram only those objects with amplitudes >1 per cent. The standard deviations of the distributions, in $\log_{10}$ units, for the open (solid) histograms are 0.25 (0.17) for the upper panel and 0.14 (0.10) for the lower panel.

6 CONCLUSIONS

We have reported on results of an *i*-band photometric survey of M50, covering ∼0.4 deg^2 of the cluster. Selection of candidate members in a V versus $V - I$ CMD using an empirical fit to the cluster sequence found 4249 candidate members, over a V magnitude range of $15.5 < V < 26$ (covering masses in the range $0.1 \lesssim M/M_{\odot} \lesssim 1.1$). The likely field contamination level was estimated using a simulated catalogue of field objects from the Besançon Galactic models (Robin et al. 2003), finding an overall contamination level of ∼47 per cent, implying that there are ∼2300 real cluster members over this mass range in our FoV.

We derived light curves for ∼63 000 objects in the M50 field, achieving a precision of <1 per cent per data point over $15 \lesssim i \lesssim 19$. The light curves of our candidate cluster members were searched for periodic modulations, presumably due to stellar rotation, giving 812 detections over the mass range $0.2 < M/M_{\odot} < 1.1$.

The rotation period distribution as a function of mass was found to show a clear mass-dependent morphology, statistically

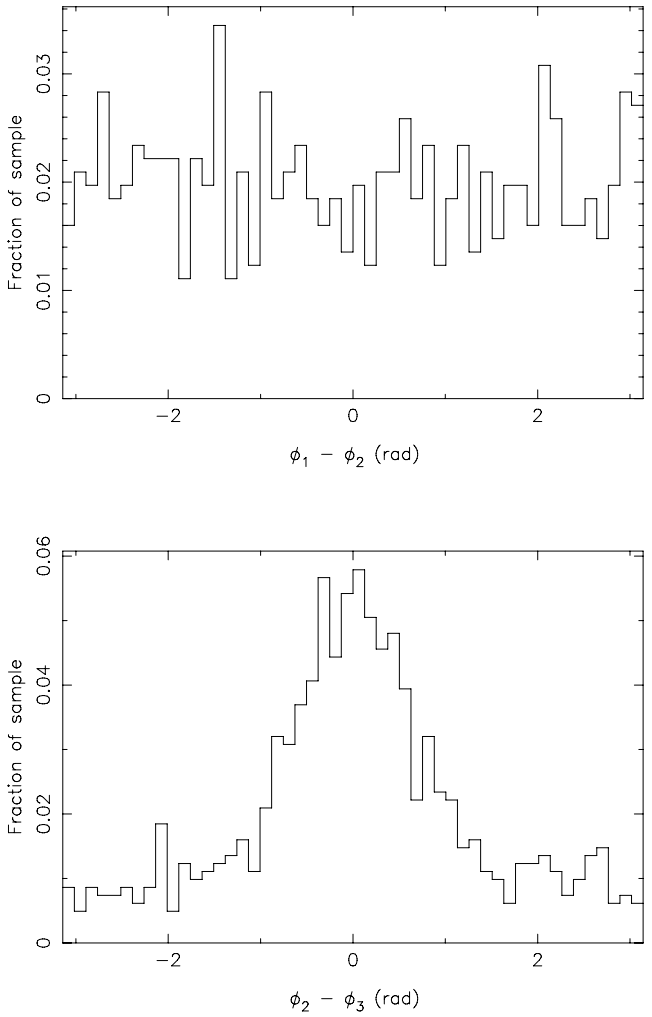

Figure 13. Histograms of the relative phase from the sine curve fitting procedure described in Section 4.1 for the second and first observing runs (upper panel), and the third and second observing runs (lower panel). The upper distribution is consistent with being uniform, indicating that the phase is essentially randomized over the 10 month time-span between the first and second observing runs. The standard deviation of the lower distribution is ∼1.0 rad.

indistinguishable from the distributions in the literature for M35 and NGC 2516 once the different mass ranges probed by the surveys are taken into account. Thus, the M50 results do not yet provide any indication of a dependence of rotation rates on cluster environment, or a 'third parameter' such as metallicity.

Finally, we demonstrated evidence that the photometric amplitudes of a significant fraction of our targets do indeed evolve over time-scales of ∼10 months, as expected (e.g. by analogy with the Sun).

ACKNOWLEDGMENTS

Based on observations obtained at CTIO, a division of the National Optical Astronomy Observatories, which is operated by the Association of Universities for Research in Astronomy, Inc., under cooperative agreement with the National Science Foundation. This research has made use of the SIMBAD data base, operated at CDS, Strasbourg, France, and the WEBDA data base, operated at the Institute for Astronomy of the University of Vienna. The Open Cluster Data base, as provided by C.F. Prosser and J.R. Stauffer, may currently be accessed at http://www.noao.edu/noao/staff/cprosser/, or by anonymous FTP to 140.252.1.11, cd /pub/prosser/clusters/.

JI gratefully acknowledges the support of a PPARC studentship, and SA the support of a PPARC postdoctoral fellowship, during the time the majority of the work was carried out. We thank the referee for his comments, which have helped to improve the paper.

REFERENCES

Aigrain S., Hodgkin S., Irwin J., Hebb L., Irwin M., Favata F., Moraux E., Pont F., 2007, MNRAS, 375, 29
Allain S., 1998, A&A, 333, 629
Baraffe I., Chabrier G., Allard F., Hauschildt P. H., 1998, A&A, 337, 403
Barnes S., Sofia S., 1996, ApJ, 462, 746
Barrado y Navascués D., Deliyannis C. P., Stauffer J. R., 2001, ApJ, 549, 452
Bouvier J., Forestini M., Allain S., 1997, A&A, 326, 1023
Claria J. J., Piatti A. E., Lapasset E., 1998, A&AS, 128, 131
Collier Cameron A., Campbell C. G., Quaintrell H., 1995, A&A, 298, 133
Currie T. et al., 2007, ApJ, 659, 599
Güdel M., 2004, ARA&A, 12, 71
Hartman J. D. et al., 2008, ApJ, in press (arXiv:0803.1488)
Hoag A. A., Johnson H. L., Iriarte B., Mitchell R. I., Hallam K. L., Sharpless S., 1961, Publ. US Nav. Obs., 17, 347
Irwin M. J., Lewis J. R., 2001, New Astron. Rev., 45, 105
Irwin J., Aigrain S., Hodgkin S., Irwin M., Bouvier J., Clarke C., Hebb L., Moraux E., 2006, MNRAS, 370, 954
Irwin J., Irwin M., Aigrain S., Hodgkin S., Hebb L., Moraux E., 2007a, MNRAS, 375, 1449
Irwin J. et al., 2007b, MNRAS, 377, 741
Irwin J., Hodgkin S., Aigrain S., Bouvier J., Hebb L., Moraux E., 2008a, MNRAS, 383, 1588
Irwin J., Hodgkin S., Aigrain S., Bouvier J., Hebb L., Irwin M., Moraux E., 2008b, MNRAS, 384, 675
Jeffries R. D., Thurston M. R., Hambly N. C., 2001, A&A, 375, 863
Jones B. F., Fischer D. A., Stauffer J. R., 1996, AJ, 112, 1562
Kalirai J. S., Fahlman G. G., Richer H. B., Ventura P., 2003, AJ, 126, 1402
Kawaler S. D., 1998, ApJ, 333, 236
Königl A., 1991, ApJ, 370, L37
Krishnamurthi A., Pinsonneault M. H., Barnes S., Sofia S., 1997, ApJ, 480, 303
Krishnamurthi A. et al., 1998, ApJ, 493, 914
Landolt A. J., 1992, AJ, 104, L340
Larson R. B., 1982, MNRAS, 200, 159
Magnitskii A. K., 1987, Soviet Astron. Lett., 13, 451
Matt S., Pudritz R. E., 2005, ApJ, 632, 135
McNamara B. J., Sekiguchi K., 1986, ApJ, 310, 613
Meibom S., Mathieu R. D., Stassun K. G., 2008, ApJ, in press (arXiv:0805.1040)
Meynet G., Mermilliod J.-C., Maeder A., 1993, A&AS, 98, 477
Perryman M. A. C. et al., 1998, A&A, 331, 81
Prosser C. F., Schild R. E., Stauffer J. R., Jones B. F., 1993a, PASP 105, 269
Prosser C. F. et al., 1993b, PASP, 105, 1407
Prosser C. F. et al., 1995, PASP, 107, 211
Queloz D., Allain S., Mermilliod J.-C., Bouvier J., Mayor M., 1998, A&A, 335, 183
Radick R. R., Thompson D. T., Lockwood G. W., Duncan D. K., Baggett W. E., 1987, ApJ, 321, 459
Robin A. C., Reylé C., Derrière S., Picaud S., 2003, A&A, 409, 523
Sagar R., Miakutin V. I., Piskunov A. E., Dluzhnevskaia O. B., 1988, MNRAS, 234, 831
Schild R., 1967, ApJ, 148, 449
Scholz A., Eislöffel J., 2004, A&A, 421, 259
Sharma S., Pandey A. K., Ogura K., Mito H., Tarusawa K., Sagar R., 2006, AJ, 132, 1669
Sills A., Pinsonneault M. H., Terndrup D. M., 2000, ApJ, 534, 335

Skumanich A., 1972, ApJ, 171, 565
Soderblom D. R., 1983, ApJS, 53, 1
Soderblom D. R., Stauffer J. R., Hudon J. D., Jones B. F., 1993, ApJS, 85, 315
Stauffer J. R., Hartmann L. W., 1987, ApJ, 318, 337
Stauffer J. R., Hartmann L., Soderblom D. R., Burnham N., 1984, ApJ, 280, 202
Stauffer J. R., Schild R. A., Baliunas S. L., Africano J. L., 1987, PASP, 99, 471
Terndrup D. M., Krishnamurthi A., Pinsonneault M. H., Stauffer J. R., 1999, AJ, 118, 1814
Terndrup D. M., Pinsonneault M., Jeffries R. D., Ford A., Sills A., 2002, ApJ, 576, 950
Terndrup D. M., Stauffer J. R., Pinsonneault M. H., Sills A., Yuan Y., Jones B. F., Fischer D., Krishamurthi A., 2000, AJ, 119, 1303
Van Leeuwen F., Alphenaar P., Meys J. J. M., 1987, A&AS, 67, 483

SUPPORTING INFORMATION

Additional Supporting Information may be found in the online version of this article:

Table 1. Properties of our 812 rotation candidates, including *V*- and *I*-band magnitudes and uncertainties from our CCD photometry, the period P, i-band amplitudes α_1, α_2, α_3 and uncertainties (magnitudes, in the instrumental bandpass), interpolated mass and radius (from the models of Baraffe et al. 1998, derived using the I magnitudes). In the table, $\sigma(x)$ denotes the uncertainty in quantity x. Note that these uncertainties do not incorporate systematic errors (e.g. in the zero-point calibration), that dominate at the bright end. Our identifiers are formed using a simple scheme of the cluster name, CCD number and a running count of stars in each CCD, concatenated with dashes. Machine-readable copies of the data tables from all the Monitor rotation period publications are also available at http://www.ast.cam.ac.uk/research/monitor/rotation/.

Please note: Wiley-Blackwell are not responsible for the content or functionality of any supporting information supplied by the authors. Any queries (other than missing material) should be directed to the corresponding author for the article.

This paper has been typeset from a TEX/LATEX file prepared by the author.